CrossMark

Weak Damping of Propagating MHD Kink Waves in the Quiescent Corona

Richard J. Morton[1] ![ORCID], Ajay K. Tiwari[1,2] ![ORCID], Tom Van Doorsselaere[3] ![ORCID], and James A. McLaughlin[1] ![ORCID]
[1] Northumbria University, Newcastle upon Tyne, NE1 8ST, UK; richard.morton@northumbria.ac.uk
[2] Centrum Wiskunde & Informatica, Amsterdam, The Netherlands
[3] Centre for mathematical Plasma Astrophysics, Department of Mathematics, KU Leuven, Celestijnenlaan 200B bus 2400, B-3001 Leuven, Belgium

Abstract

Propagating transverse waves are thought to be a key transporter of Poynting flux throughout the Sun's atmosphere. Recent studies have shown that these transverse motions, interpreted as the magnetohydrodynamic kink mode, are prevalent throughout the corona. The associated energy estimates suggest the waves carry enough energy to meet the demands of coronal radiative losses in the quiescent Sun. However, it is still unclear how the waves deposit their energy into the coronal plasma. We present the results from a large-scale study of propagating kink waves in the quiescent corona using data from the Coronal Multi-channel Polarimeter (CoMP). The analysis reveals that the kink waves appear to be weakly damped, which would imply low rates of energy transfer from the large-scale transverse motions to smaller scales via either uniturbulence or resonant absorption. This raises questions about how the observed kink modes would deposit their energy into the coronal plasma. Moreover, these observations, combined with the results of Monte Carlo simulations, lead us to infer that the solar corona displays a spectrum of density ratios, with a smaller density ratio (relative to the ambient corona) in quiescent coronal loops and a higher density ratio in active-region coronal loops.

Unified Astronomy Thesaurus concepts: Magnetohydrodynamics (1964); Solar corona (1483); Solar coronal waves (1995); Solar coronal heating (1989); Quiet solar corona (1992); Solar coronal loops (1485)

1. Introduction

It is now well established that transverse wave modes are ubiquitous throughout the Sun's atmosphere. The most unambiguous signature of these waves is the transverse displacement of magnetized waveguides, observed in both the chromosphere (e.g., fibrils, Morton et al. 2012, 2014; Jafarzadeh et al. 2017; super-penumbral fibrils, Morton et al. 2021; spicules, Okamoto & De Pontieu 2011) and corona (e.g., Tomczyk et al. 2007; McIntosh et al. 2011; Thurgood et al. 2014; Morton et al. 2019; Yang et al. 2020). This motion has been interpreted from magnetohydrodynamic (MHD) wave theory as the kink mode (e.g., Van Doorsselaere et al. 2008). Within the corona, there appear to be three common variants of the kink mode identified: the rapidly damped standing mode (e.g., Aschwanden et al. 1999; Nakariakov et al. 1999; Goddard et al. 2016), the decayless standing mode (e.g., Nisticò et al. 2013; Anfinogentov et al. 2015; Karampelas & Van Doorsselaere 2020), and the propagating mode (Tomczyk & McIntosh 2009; Morton et al. 2015, 2016). The propagating kink mode is found throughout the corona (Morton et al. 2019; Yang et al. 2020), and energy estimates suggest the waves are powerful enough to meet the heating rate required to balance the radiative losses in the quiescent corona and coronal holes (McIntosh et al. 2011; Weberg et al. 2018). On the other hand, the damped standing mode is excited by impulsive events and occurs too infrequently to provide a significant energetic contribution (Terradas & Arregui 2018; Nakariakov & Kolotkov 2020). For the decayless variant, the situation is less clear: they have only been detected in active regions, but Hillier et al. (2020) find that their energy content is potentially insufficient to meet active-region heating

requirements. The connection between the decayless standing mode and the propagating kink mode, if any, is still unclear. Interestingly, the nature of some of the events classified as standing kink modes has been called into question (Hindman & Jain 2014; Jain et al. 2015), with the suggestion that a number of the observed cases may arise as the response of a magnetic arcade to a fast wave disturbance propagating obliquely to the magnetic field.

2. Kink Waves

In order to provide the necessary context for our later analysis and discussions, we provide a summary of some of the key observational and theoretical results for kink modes. While the new results presented later are focused on the propagating kink modes, we draw comparisons to the standing modes.

2.1. Propagating Kink Waves

The propagating kink waves have largely been observed with Doppler velocity measurements of the 1074.7 nm Fe XIII line from the Coronal Multi-Channel Polarimeter (CoMP; Tomczyk et al. 2008), with recent studies clearly showing they exist throughout the corona (Morton et al. 2019; Yang et al. 2020). It appears that the waves propagate along coronal structures (e.g., loops, plumes) that are overdense compared to the ambient plasma, with the overdensity signified by enhanced emission in coronal EUV emission lines. The waves propagate at speeds between 300 and 700 km s^{-1} (Morton et al. 2016; Yang et al. 2020), which is significantly greater than the typical coronal sound speed. The power spectra of velocity fluctuations demonstrate power-law behavior over the currently observable frequency range (10^{-4}–10^{-2} Hz; Morton et al. 2016). There is also an enhancement of the wave power centered on 4 mHz that has a direct correspondence to the transverse displacements of

coronal structures observed with the Solar Dynamics Observatory (SDO) (Morton et al. 2019).

The modeling of MHD waves in coronal structures is typically simplified to assume an overdense waveguide with a cylindrical cross-sectional geometry (e.g., Spruit 1982; Edwin & Roberts 1983). The velocity fluctuations observed in CoMP (and transverse displacements observed in SDO) are then interpreted as the kink mode. In the long-wavelength limit, the kink mode is Alfvénic in nature (Goossens et al. 2009, 2012), and the phase speed is given by

$$c_k^2 = \frac{B_i^2 + B_e^2}{\mu_0(\rho_i + \rho_e)},$$ (1)

which depends upon the local magnetic field, B, and density, ρ. The subscripts refer to the internal, i, and external, e, plasma quantities, and μ_0 is the magnetic permeability. The long-wavelength regime occurs when $kR \ll 1$, where $k = 2\pi/\lambda$ is the wavenumber (λ the wavelength) of the wave and R is the radius of the waveguide.[4] Given that the typical radius of coronal loops is ~ 1 Mm (Brooks et al. 2013; Williams et al. 2020) and the wavelengths for the propagating kink modes are $\lambda = c_k/f = 30$–7000 Mm (where f is the frequency), the observed kink waves are comfortably in the long-wavelength regime.

2.2. Wave-damping Theory

If the propagating kink modes are to play a relevant role in heating the corona, the waves have to dissipate the energy they transport into the plasma. In order for this to occur, the energy is required to be transferred to smaller spatial scales than those currently associated with the observed waves. A mechanism that has received considerable renewed interest recently is phase mixing (Pritchett & Dawson 1978; Heyvaerts & Priest 1983).

The density contrast between the internal and external plasma of the coronal structures leads to a gradient in the Alfvén speed across the waveguide boundary. The spatially varying Alfvén frequency in the boundary layer enables phase mixing of rotational motions, which are described by Alfvén waves, and hence creates small spatial scales that eventually enable dissipation of the wave energy (e.g., Soler & Terradas 2015; Pagano & Moortel 2017; Pagano et al. 2020). Moreover, a resonance is created at the locations where the Alfvén frequencies in the boundary layer match that of the global kink frequencies. A consequence of the resonance is the energy in the transverse motions is transferred to rotational motions via resonant absorption (e.g., Ionson 1978; Ruderman & Roberts 2002; Terradas et al. 2010; Goossens et al. 2011) and effectively couples the kink and Alfvén modes (Pascoe et al. 2010, 2012).

The rate of damping for the propagating kink mode via resonant absorption in the thin-boundary limit is given by (see, e.g., Terradas et al. 2010)[5]

---

[4] For clarity, we assume that the density of the waveguide is inhomogeneous but smoothly varying perpendicular to the magnetic field. Then R is defined as being at the location where $\rho(R)$ is equal to density averaged over R.

[5] Similarly, for a standing kink mode, the left-hand side is replaced by the temporal rate of damping τ_{RA}/P, where τ_{RA} is the damping rate and P is the period (Ruderman & Roberts 2002).

$$\frac{L_D}{\lambda} = \frac{2}{\pi} \frac{R}{l} \frac{\rho_i + \rho_e}{\rho_i - \rho_e}.$$ (2)

Here, L_D is the spatial damping length, and l is the length scale of the inhomogeneous boundary layer. The factor $2/\pi$ comes from assuming a sinusoidal density profile across the boundary layer. The resonant damping of kink modes can be viewed as a linear mechanism for energy transfer, in the sense that it occurs in linearized MHD. This is readily seen in Equation (2) where the damping is independent of amplitude.

More recently, it has been suggested that large-amplitude kink waves can be damped by a nonlinear mechanism, the so-called "uniturbulence" (Magyar et al. 2017, 2019; Van Doorsselaere et al. 2020) that causes a self-cascade of the wave energy. Van Doorsselaere et al. (2020) has computed the nonlinear evolution of standing and propagating kink waves with Elsässer variables in order to understand their nonlinear damping as a consequence of the Kelvin–Helmholtz instability (KHI; see, e.g., Terradas et al. 2008; Antolin et al. 2014; Magyar & Van Doorsselaere 2016) or uniturbulence (Magyar et al. 2017, 2019). They predicted that damping times can be the same order of magnitude as those expected from resonant absorption for propagating waves. As with resonant absorption (and subsequent phase mixing), the key form of the inhomogeneity for uniturbulence is related to the presence of field-aligned density enhancements (i.e., overdense waveguides) and is suggested to be a form of generalized phase mixing (Magyar et al. 2019).

The timescale for the energy cascade rate, τ_{Pr}, in propagating waves is given by Van Doorsselaere et al. (2020), and recasting their damping for energy to velocity damping:

$$\tau_{Pr} = 2\sqrt{5}\pi \frac{2R}{\delta v} \frac{\rho_i + \rho_e}{\rho_i - \rho_e} = 2\sqrt{5}\pi \frac{P}{2\pi a} \frac{\rho_i + \rho_e}{\rho_i - \rho_e},$$ (3)

with δv the velocity amplitude of the kink mode. The presence of δv in Equation (3) highlights the dependence on the kink-mode amplitude. The second form of the timescale is written in terms of a normalized amplitude, $a = A/R$, given that $\delta v = 2\pi A/P$ (where A is the displacement amplitude and P the wave period). The exact interplay between the resonant absorption and uniturbulence mechanisms in kink-wave damping is still unclear. There is a likely competition between both methods in damping the kink modes, with uniturbulence playing a dominant role when the wave amplitude is significantly large. As yet, a full comparative study does not exist.

2.3. Observed Wave Damping

While it is currently somewhat difficult to measure the development of small scales and the subsequent dissipation of wave energy, an estimate of the rate of damping of kink waves is currently feasible.

There are now many observational examples of the damped standing kink mode in active-region loops (e.g., Aschwanden et al. 2002; Verwichte et al. 2004), which appear well described by resonant damping (e.g., Goossens et al. 2002; Ruderman & Roberts 2002; Aschwanden et al. 2003). Goddard et al. (2016) has compiled a catalog of damped standing kink waves, which was later extended by Nechaeva et al. (2019) to include 223 oscillation events. From this catalog, the rate of wave damping (τ_{RA}/P) is typically <10, with a mean of 2.3 (see Section 3 for details). Goddard & Nakariakov (2016) presented a

meta-analysis of a number of standing kink modes cases, which suggested there was a dependence on the damping rate with respect to the amplitude of the oscillation. Given that resonant damping is independent of amplitude (see Equation (2)), the results could indicate the action of a nonlinear damping mechanism for large-amplitude kink waves.

Relevant to our work, Verwichte et al. (2013) demonstrated the potential of utilizing statistical approaches that forward-model the damping of kink waves in order to constrain the cross-sectional characteristics of the coronal loops. The essence of their approach was to generate physical properties of the coronal loop (e.g., density contrast, length scale of the inhomogeneous layer) by randomly drawing values from assumed distributions, which were fed through analytical expressions for resonant damping. This enabled synthetic distributions of damping times to be generated that could be compared to an empirical distribution of 50 existing cases. Distributions of loop parameters were optimized to improve the fit between synthetic and empirical distributions.

Recently, Van Doorsselaere et al. (2021) took a similar approach, although focused on the modeling of the nonlinear damping of the standing kink waves (incorporating an analytic expression for the nonlinear damping, i.e., Equation (5)). The damping times were matched with the simulation results of Magyar & Van Doorsselaere (2016) and the empirical damping times from the catalog of Nechaeva et al. (2019). They obtained a good agreement between the Monte Carlo simulations of damping times in loop models and the observations, suggesting that the observed amplitude-dependent damping is a consequence of the A^{-1} scaling present in the expression for damping rates (see Equations (3) and (5)).

Up until now, there have only been a few observations of damped propagating coronal kink. In fact, they have been restricted to a single case observed with CoMP that was originally reported by Tomczyk & McIntosh (2009). Verth et al. (2010) demonstrated the damping for the event was frequency dependent and noted the observed behavior was described well by resonant absorption (Terradas et al. 2010). Further, Verth et al. (2010) suggested the ratio of the power for outward to inward propagating kink waves, namely

$$\langle P(f) \rangle_{\mathrm{ratio}} = \frac{P_{\mathrm{out}}}{P_{\mathrm{in}}} \exp\left(\frac{2L}{v_{\mathrm{ph}} \xi_{\mathrm{E}}} f\right), \qquad (4)$$

should provide a reasonable model in order to measure the damping rate for propagating waves. Here L is the loop length, ξ_{E} is referred to as the quality factor or equilibrium parameter, v_{ph} is the phase speed, P_{out} is the power of waves propagating upwards, and P_{in} is the power of the waves propagating inwards. This expression[6] is general and applicable for any mechanism where the damping is exponential in nature (c.f. Hood et al. 2013 for a discussion of the Gaussian-damping regime in resonant absorption). Other studies have also used this single example of the damped propagating kink wave, interpreting the observed frequency-dependent damping as resonant absorption (Verwichte et al. 2013; Pascoe et al. 2015; Montes-Solís & Arregui 2020). Recently, Tiwari et al. (2019) demonstrated that some of these previous studies likely

underestimate the damping length by erroneously assuming the generative distribution for the power ratio is described by a Gaussian distribution (applicable when fitting Equation (4) to the power spectrum obtained from CoMP data).

The preceding discussion highlights the need to measure the rate of damping for propagating kink waves. It is a key piece of information required to substantiate the role of resonant absorption, phase mixing, and/or uniturbulence in the heating of the quiescent corona. Such measurements place a limit on the rate of energy transfer from the global kink modes to the smaller scales, subsequently influencing the rate of heating. While only suggestive, Tiwari et al. (2019) found that the quality factor for quiescent coronal loops was large compared to the typical values found in active-region loops. Furthermore, the damping rates can also be used for magnetoseismology, enabling the cross-sectional properties of coronal loops to be inferred. Here we extend this previous analysis and present the key result of a larger study of propagating kink waves in quiescent coronal loops.

3. Observations and Data Analysis

All data used within this study were taken with the CoMP instrument between the dates of 2012 January 20 and 2014 January 2. Details of individual data sets used are given in a companion publication, Tiwari et al. (2021), which discusses the catalog of events in more detail. The data were processed using the standard CoMP reduction pipeline and the Doppler velocity products are utilized. Additional registration of the data with cross-correlation is undertaken to achieve subpixel alignment of time sequences for individual days. Full details of the registration process are discussed in Morton et al. (2016). The subsequent analysis of the data is described fully in Tiwari et al. (2019, 2021), although we give a brief overview here.

We restrict our attention to quiescent coronal loops, avoiding active regions. In order to minimize geometric influences on the measurements, e.g., foreshortening, the coronal loops that are selected for analysis are oriented such that the longitudinal axis is close to being in the plane of sky. Time–distance diagrams are obtained that follow the direction of wave propagation along the coronal loops (e.g., Tomczyk & McIntosh 2009; Morton et al. 2015; Tiwari et al. 2019). For each of the time–distance diagrams, a two-dimensional Fourier transform is applied to separate the outward and inward propagating wave components. The power spectra in frequency–wavenumber space are then obtained. Summing over wavenumber and taking the ratio of the outward to inward waves provide the power ratio as a function of frequency. The power ratio is then fit with the exponential model given in Equation (4) using maximum likelihood, assuming the power ratio is distributed about the true value following an F-distribution (see Tiwari et al. 2019 for full details of the maximum likelihood approach).

In order to estimate the equilibrium parameter, ξ_{E}, for each loop, we are required to measure the propagation speed of the waves. This is achieved via a coherence analysis of the velocity time series that make up each time–distance diagram (Tomczyk & McIntosh 2009; Tiwari et al. 2019). In all, we provide estimates for the rate of damping of propagating kink waves in 77 quiescent coronal loops, which is shown in Figure 1. The density distribution of the equilibrium parameter is estimated with kernel density estimation (KDE) using a Gaussian kernel. The bandwidth parameter is selected via cross-validation.[7]

---

[6] Equation (4) also assumes that the power ratio is averaged along half of the coronal loop. Tiwari et al. (2019) provide an alternative for this expression when only a section of the loop is used to measure the power ratio.

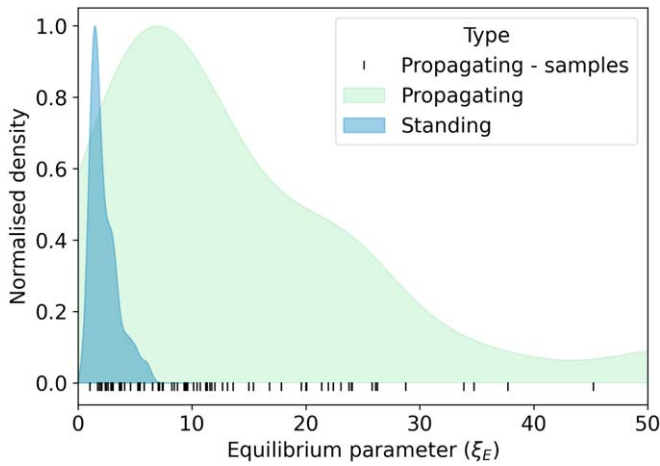[7] Performed with Scikit-learn (Pedregosa et al. 2011).

Figure 1. Distribution of equilibrium parameter for propagating kink waves in 77 quiescent coronal loops. The plot shows the kernel density estimation for the distribution, with the individual samples indicated by the vertical marks at the bottom of the plot. Six values for ξ_E are greater than 50 and are not shown in the graph for visualization purposes. For comparison, the distribution of ξ_E for damped standing kink waves measured in active regions is also shown. The two density distributions are both normalized to further aid visualization.

To provide some perspective for the equilibrium parameters from propagating kink waves in quiescent coronal loops, we also calculate the equilibrium parameter for the damped standing kink waves observed in coronal loops in active regions. The data for the active-region coronal loops and wave parameters are taken from the catalog of standing kink modes given in Nechaeva et al. (2019). The equilibrium parameter for the standing modes is calculated by taking the ratio of the estimated damping time by the period. The results are shown in Figure 1. Catalog entries without a period or damping time estimate are excluded, leaving 101 samples.

4. Weak Damping in the Quiescent Sun

The most significant conclusion that can be drawn from the distribution of equilibrium parameters (Figure 1) is that the propagating kink waves in the quiescent Sun are weakly damped. This conclusion is made starkly clear in comparison to the corresponding values for the (rapidly damped) standing kink modes. The values of the equilibrium parameter for the propagating waves are in the range $0.9 < \xi_E < 298$. This range is significantly broader than that of the equilibrium parameters for standing waves ($0.7 < \xi_E < 7$). The central tendencies of the two sets of samples are also different, with the propagating waves having a mean value of 24 ± 4 (median 11) and the standing waves having a mean 2.3 ± 0.1 (median 1.8); the uncertainties given are standard errors.

Assuming that the dominant mechanism for the observed kink-wave damping is resonant absorption, the implication of the large equilibrium parameter values is that the quiescent loops must be physically different from those found in active regions. This is perhaps not such a surprise. From Equation (2), it is seen that the value of the equilibrium parameter is determined by the difference in densities between the internal and external plasma (although not the magnitude of the density). Consequently, the density ratio of loop plasma to ambient plasma (ρ_i/ρ_e) is smaller in quiescent loops, relative to active-region loops.

The other quantity in Equation (2) is the relative size of the inhomogeneous boundary layer, l/R, which results from an approximation to the gradient of density across the inhomogeneous layer, namely $|d\rho/dr|$ (e.g., Goossens 2008). It was shown by Arregui & Goossens (2019) that the variation of density across the inhomogeneous layer can be factored into a single quantity (which they denote G) and is essentially a shape factor that "relates the local variation of density at the resonant position to the global variation of the density over the mean radius of the cylinder." The overall value of this quantity G can influence the size of ξ_E, and it likely takes a range of values across different coronal structures. However, we see no reason why the distribution of G values would be different for quiescent and active-region loop populations.

In our opinion, this places a focus on the density ratio as the underlying factor determining the differences in the strength of damping between the quiescent loops and active-region loops. Hence, the inference is that active-region loops are denser than quiescent loops, relative to the ambient plasma. This has support from work on coronal loop thermodynamics. Under the uncontroversial assumption that active-region loops have a greater heating rate than quiescent loops, active-region loops are expected to be denser (see, e.g., the scaling law, Equation (45), for coronal densities in Bradshaw & Emslie 2020).

A similar inference can be drawn if uniturbulence dominates the damping. Equation (3) shows that the rate of energy transfer has the same dependence on the density contrast. However, the damping rate is also influenced by $R/\delta v$.

In order to examine the role of the density contrast and the roles of resonant absorption/uniturbulence further, we undertake a Monte Carlo forward-modeling approach. The general approach follows that of Verwichte et al. (2013) and Van Doorsselaere et al. (2021), where values for ξ_E are generated by the random sampling of coronal loop parameters and observed wave parameters, then feeding those values through analytical expressions of damping rates. The following subsections provide the details for the modeling.

4.1. Assumptions and Equations

The models that describe the physics within the coronal loops are the same as those in Van Doorsselaere et al. (2020, 2021). The coronal loops are assumed to consist of a straight cylinder with radius R embedded in a uniform magnetic field with a low β. The internal density ρ_i is higher than the external density ρ_e, resulting in a density contrast $\zeta = \rho_i/\rho_e$. The loop is oscillating with a period P and a displacement amplitude A.

The damping for the propagating waves by uniturbulence is given in Equation (3), while the damping for standing waves by the KHI development, τ_{St}, was derived in Van Doorsselaere et al. (2021) (taking into account the erratum) and is given by

$$\tau_{St} = 40\sqrt{\pi}\frac{P}{2\pi a}\frac{1+\zeta}{\sqrt{\zeta^2 - 2\zeta + 97}}. \quad (5)$$

Furthermore, we utilize the expression for the damping time of resonant absorption, τ_{RA}, for standing modes given by Ruderman & Roberts (2002), which was derived in the thin-tube, thin-boundary limit, and which assumed a sinusoidal density profile in the inhomogeneous layer[8] with width l. This expression is similar to Equation (2), with the left-hand side equal to τ_{RA}/P. For propagating waves, we consider

---

[8] It is worth mentioning that the formulae for the nonlinear damping $\tau_{St,Pr}$ consider a step function in density instead.

Equation (2) and assume that damping length and damping time are closely related:

$$\xi_{RA} = \frac{L_D}{\lambda} = \frac{\tau_{RA}}{P},$$ (6)

which is correct for weak damping but not true in general in complicated dispersion relations. Here we denote the equilibrium parameter for resonant absorption as ξ_{RA}.

Following the approach of Van Doorsselaere et al. (2021), we combine the damping of resonant absorption with the nonlinear damping through the formula:

$$\exp\left(-\frac{t}{\tau}\right) = \exp\left(-\frac{t}{\tau_{St,Pr}}\right)\exp\left(-\frac{t}{\tau_{RA}}\right),$$ (7)

allowing us to express the total damping with τ as the harmonic average:

$$\frac{1}{\tau} = \frac{1}{\tau_{St,Pr}} + \frac{1}{\tau_{RA}}.$$ (8)

Taking the harmonic average is a typical approach if the damping of two mechanisms is small and independent (and thus additive). This is likely satisfied for the propagating waves, but the assumptions are violated for the standing modes where there is strong damping (and the presence of resonant absorption kickstarts the nonlinear damping; see Antolin & Van Doorsselaere 2019). Still, it is a first-order approach to the combination of both damping mechanisms and needs revision in the future.

In the following, we use the equilibrium parameter, rather than the damping time, as it is independent of frequency for both resonant absorption and nonlinear damping. Multiplying Equation (8) by the period, we define the total equilibrium parameter as

$$\frac{1}{\xi_{E,Total}} = \frac{1}{\xi_{NL}} + \frac{1}{\xi_{RA}}.$$ (9)

The equilibrium parameter for the nonlinear damping is denoted ξ_{NL}.

4.2. Physical parameters

In order to simulate the damping rates using the above equations, we need to specify the latent values for the density contrast, width of the inhomogeneous layer, and loop radius.[9] Moreover, we also require the typical amplitudes of oscillations. We discuss our choices next and a summary is given in Table 1.

Propagating wave amplitude (A). While we are able to estimate the kink-wave damping with CoMP, the limited spatial resolution of the instrument means that observed wave amplitudes are reduced due to spatial averaging and line-of-sight integration (see, e.g., De Moortel & Pascoe 2012; McIntosh & De Pontieu 2012; Pant et al. 2019). Hence, we use measurements of the transverse displacements of loops in the quiescent Sun observed with the SDO Atmospheric Imaging Assembly (AIA; Lemen et al. 2012) in the 171 Å

Table 1
Physical Parameters for Forward Modeling

Parameter	Range	Distribution
ζ standing	1–5	$\mathcal{U}(1, 5)$
ζ propagating	1–1.3	$\mathcal{U}(1, 1.3)$
l/R	0–2	$\mathcal{U}(0, 2)$
Loop radius (R)	0.5–10 Mm	$\mathcal{U}(0.5, 10)$

channel, taking the values of the amplitude discussed in Morton et al. (2019). The data set contains 590 values.

Standing-wave parameters (A). The standing-kink-mode amplitudes are taken from the catalog of Nechaeva et al. (2019), which represents kink waves in active-region coronal loops measured with SDO/AIA. The catalog contains 223 values.

Loop radii (R). The radius of coronal loops is a well-discussed topic. Past investigations have focused largely on active-region coronal loops, in part due to their high visibility in coronal EUV images. Aschwanden & Peter (2017) provide a detailed investigation of active-region coronal loop widths using AIA and Hi-C, along with a summary of all previous observations to date (results from the more recent Hi-C 2.1 mission can be found in Williams et al. 2020 and are in agreement). They report that the widths of coronal loops peak at 0.5 Mm but can be as large as 10 Mm. However, the resolved loops observed with AIA have a larger peak at $\sim$1.2 Mm, which may better represent the coronal loops in which the standing kink modes are found. To date, there are no similar measurements for quiescent loops, and for now, we assume that the widths are similar. For this study, we assume the loop widths are uniformly distributed with $R = [0.5, 10]$ Mm. The impact of choosing a uniform distribution over this range means that we are selecting larger loop radii more often than observed. This will lead to an underestimate of the strength of nonlinear damping.

The remaining parameters are latent variables in the model, namely ζ and l/R. There have been numerous efforts in the past to determine the size of the density contrast and the width of the inhomogeneous layers in coronal loops using coronal seismology (e.g., Aschwanden et al. 2003; Arregui & Ramos 2011; Ramos & Arregui 2013; Verwichte et al. 2013; Goddard et al. 2017; Pascoe et al. 2018). The focus of these attempts has exploited only standing modes in active-region loops, and so the estimated values of the density contrast naturally reflect the conditions of active-region loops. Moreover, each of them has assumed only resonant absorption is in action, which will likely influence the estimated values.

Width of the inhomogeneous layer (l/R). The inhomogeneous layer can be in the range $l/R = [0, 2]$, and the above studies generally favor larger values of the inhomogeneous layer, suggesting the resonant layer is thick. We take a more conservative approach and assume the values are drawn uniformly from the range. If the true values of l/R are typically toward the larger end of this range, the impact of our choice will be to underestimate the strength of the resonant damping.

Density contrast (ζ). The results across the previous studies are relatively consistent, with the majority of values in the range $\zeta = [1, 10]$. However, the estimates tend to have a preference for small values ($\zeta < 5$). Hence, in the active-region loop model, we choose to draw values uniformly in the range $\zeta = [1, 5]$.

---

[9] In principle one could measure the loop radii for the standing modes with AIA, but we do not undertake that here. In the CoMP data, the velocity signal is averaged over neighboring loops due to spatial resolution; hence a single radius cannot be associated with the observed kink waves.
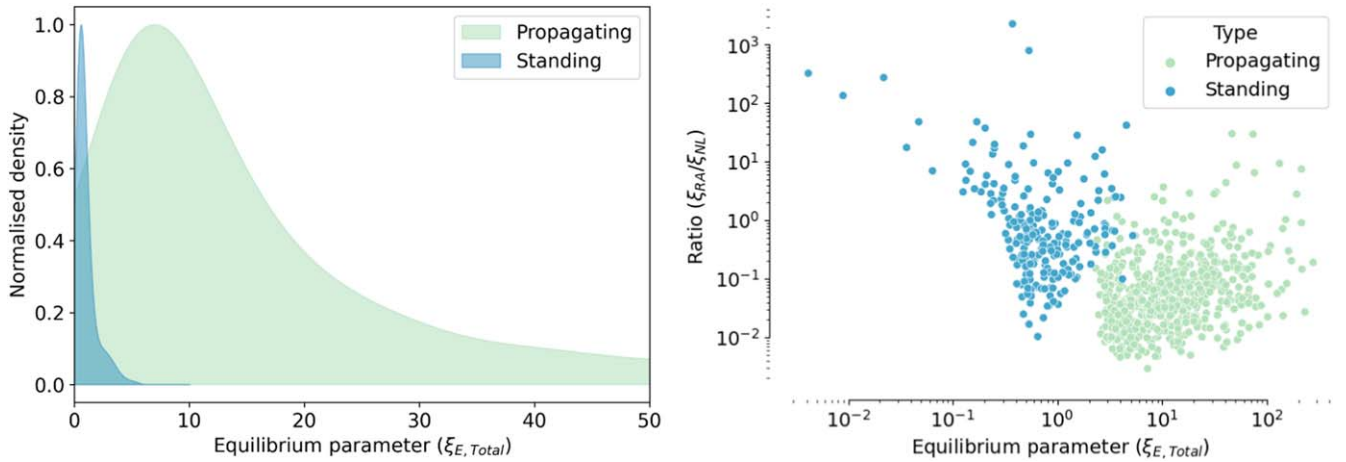
Figure 2. Results from the Monte Carlo simulations. The left panel shows the simulated distributions of equilibrium parameters. The right panel reveals the contributions of resonant absorption (ξ_{RA}) and nonlinear damping (ξ_{NL}) in the overall damping ($\xi_{E,Total}$) of both wave modes.

For the coronal loops in the quiescent Sun, which support the propagating kink waves, to our knowledge, there have been no previous estimates. It might be natural to expect that the density of the quiescent loops is closer to the ambient coronal value for two reasons. The first is that the quiescent loops' visible contrast in EUV images is lower than their active-region counterparts, suggesting similar densities and temperatures to the ambient corona. Second, the required heating rate is at least five times smaller in the quiescent Sun. This would imply that the energy released (through whichever mechanism) is less and, as such, there is less energy available to contribute to ablating the transition region and chromosphere and reducing evaporation of the denser plasma into the loops (e.g., Cargill et al. 2012). Given the unknown nature of ζ in the quiescent Sun, we leave this as a free parameter that we vary in order to obtain a reasonable match between simulations and the observed data.

4.3. Monte Carlo Approach

For each of the observed cases (both propagating and standing), we select a value of wave amplitude. This is deprojected by using a randomly drawn angle between $\phi = [-\pi/2 + \delta\phi, \ \pi/2 - \delta\phi]$ to compute $A_{\mathrm{deproject}} = A/\cos\phi$, with the assumption that the oscillation plane is oriented randomly with respect to the line of sight. The $\delta\phi$ is intended to represent a limit on the orientation of the displacement, beyond which the oscillation is essentially along the line of sight and cannot be measured by imaging instruments. Here we set $\delta\phi = \pi/18$. We also take a realization of the width of the inhomogeneous layer (l/R), density contrast (ζ), and radius (R) drawn from the appropriate distributions.

The only free parameter that we have in models is the range of ζ for the quiescent coronal loops. As mentioned there are no previous measurements to guide us. Hence, we vary the upper value of ζ until various moments and statistics of the observed and simulated distributions are in rough agreement. In particular, we examined the mean, median, mode, variance, skew, and kurtosis. This led to the range $\zeta = [1, 1.3]$, and the resulting distributions for $\xi_{E,\ Total}$ are shown in Figure 2. The values of the moments/statistics are given in Table 2 for the observed distribution and also for the Monte Carlo results for the given range of ζ (means and standard deviations of values calculated from 1000 different simulations). For reference, increasing the maximum value of ζ to 2 leads to significantly smaller values of

Table 2
Observed vs. Simulated Distributions of ξ for Propagating Waves

	Observed	Monte Carlo
Mean	24	23 ± 1.5
Median	11	10 ± 0.6
Mode	5	7.0 ± 0.3
Std. Dev.	39	35 ± 3
Skew	4.6	3.7 ± 0.3
Kurtosis	27	17 ± 3
Max value	298	275 ± 22
Min value	1.05	2.0 ± 0.3

mean, median, and mode than observed, and to larger values of skew and kurtosis. We note that the range of ζ is not optimized but chosen by hand and could probably be more finely tuned by minimizing some objective function that evaluates a measure of distance between the observed and simulated distribution. However, our goal here is to demonstrate the idea that, assuming resonant and/or nonlinear damping, density contrast is responsible for the larger values of the equilibrium parameter, rather than to tune the model parameters.

4.4. Results

Figure 2 shows the results from the forward modeling. We first focus on the distribution of the simulated equilibrium parameter, ($\xi_{E,Total}$—shown in the left panel), which we assume is comparable to the observed values of ξ_E. Comparing Figures 2 and 1 reveals a remarkable agreement for propagating waves. Even with relatively conservative assumptions about key physical parameters and the ability to "tune" one parameter, the model can provide a reasonable description of the observed distribution of the equilibrium parameter. We are able to match the aforementioned moments and statistics of the observed distribution reasonably well (Table 2), hence the visible agreement between density distributions. We stress that we are not suggesting that, in the quiescent corona, the largest value of $\zeta = 1.3$. The modeling used a uniform distribution for ζ but it is possible that a skewed, long-tailed distribution for ζ (i.e., with occasional larger values of ζ) could also be feasible.

The simulated distribution for the standing modes is narrower with smaller measures of central tendency, i.e., the model provides equilibrium parameters that are smaller than observed.

This is likely due to the assumptions in the model not holding in the strong damping regime. However, we do not focus on these differences further given our focus is on the propagating waves.

It is also informative to look at the role the two different damping mechanisms play in total damping. In order to investigate this, we show the ratio of the resonant damping equilibrium parameter to the nonlinear damping equilibrium parameter, i.e., ξ_{RA}/ξ_{NL}. This quantity is compared to the total equilibrium parameter on the right-hand panel of Figure 2. It can be seen for the propagating waves that, generally, $\xi_{RA}/\xi_{NL} < 1$, which means that resonant damping dominates over nonlinear damping. This result will depend on the wave amplitude, which in turn depends on the frequency (Morton et al. 2019). The situation is different for standing modes, where nonlinear damping appears to play an equivalent or greater role in the overall wave damping.

5. Discussion

The damping of propagating kink waves in the quiescent corona is found to be weaker than the damping of the standing kink modes in active regions. Both our intuition and the results of the forward modeling support the role of the density contrast playing a key role in the damping of kink waves in the quiescent Sun. We note that the forward modeling assumes the other physical aspects of coronal loops, i.e., transverse homogeneity length scale and radius, are similar for active-region and quiescent loops. Of these three parameters, we can only motivate a physical reason for the density contrast differing between the two sets of loops.

We believe it is also worth mentioning the observations of propagating kink waves along magnetized plasma structures in coronal holes. While the structures in coronal holes are not loops, they still appear (marginally) brighter in EUV emission than the ambient plasma (e.g., Morton et al. 2015), implying they are also overdense, although less so than active-region loops and quiescent loops. This property is reflected in the observed wave behavior. It has been shown in Morton et al. (2015) and Weberg et al. (2020) that the propagating kink waves in coronal holes demonstrate an increase in amplitude that is consistent with expectations from WKB wave propagation in a gravitationally stratified plasma (at least below $1.3\,R_\odot$), i.e., there is no evidence for wave damping.[10]

Hence, if the density contrast between the waveguide and the ambient plasma is the main factor behind the differences in observed damping rates between standing kink modes in active regions and propagating kink waves in the quiescent corona (and in coronal holes), this would indicate the magnetized waveguides display a spectrum of density ratios. The largest density ratios occur in active-region loops (leading to the observed rapid damping of the kink waves) and the smallest in coronal hole waveguides (leading to no observable wave damping).

The arguably more significant implication of the observed weak damping is that the rate of energy transfer from the global kink motion to azimuthal motions is low. This potentially rules

out the energy pathway of resonant absorption to phase mixing as a viable mechanism for dissipating the kink-wave energy in the quiescent corona. The numerical studies of Pagano & Moortel (2017), Pagano & De Moortel (2019), an Pagano et al. (2020) appear to show that phase mixing is inefficient for heating even when the rate of energy transfer is likely at its largest, i.e., under active-region conditions. Moreover, the rate at which small scales develop due to phase mixing is governed by the density gradient through the inhomogeneous boundary layer. This can be seen in an approximate expression for the length scale due to phase mixing, L_{pm}, given by Mann et al. (1995):

$$L_{pm} = \frac{2\pi}{|d\omega_a(r)/dr|t}, \tag{10}$$

where $\omega_a(r)$ is the Alfvén frequency across the inhomogeneous boundary layer.[11] Hence, smaller density ratios in the quiescent coronal loops (relative to active-region loops) will not only reduce the rate of transfer of energy from the global kink mode to the Alfvén modes but also delay the development of the small scales due to phase mixing.

The role of the nonlinear damping due to uniturbulence appears to be less than resonant damping (as suggested from the forward modeling), so this will also play a small role in wave damping in the quiescent Sun.

The observed weak damping and implication of inefficient energy transfer to small spatial scales mean that we currently find it difficult to see how phase mixing can play an important role in dissipating kink -wave energy in the quiescent corona. This result would naturally extend to the waveguides in coronal holes also. However, this does not rule out the propagating kink waves as a key player in the heating of the quiescent corona. There are still a number of potential mechanisms that might be able to dissipate the wave energy. A leading candidate from wave-based heating is Alfvénic turbulence, which has had some success in producing heated coronal loops (Buchlin & Velli 2007; van Ballegooijen et al. 2011, 2017) and also in producing a hot, fast solar wind (e.g., Cranmer et al. 2007; Shoda et al. 2018, 2019). The current models ignore the perpendicular density structure and so do not contain kink modes; however, the Alfvénic nature of the low-frequency kink modes suggests they could also be susceptible to the same nonlinear interactions that occur between counterpropagating waves and transfer energy to smaller scales. We eagerly await the results of an Alfvénic turbulence model that would include the structured nature of the lower solar corona and would shed light on the dissipation of the wave energy in kink modes.

Finally, the weak damping rates estimated from this work raise a puzzling question: Why do we not see any evidence for resonant frequencies in the loops studied in the CoMP data? The standard picture of wave propagation through the Sun's atmosphere suggests that the Alfvénic waves in the corona will be reflected off the transition region due to steep gradients in Alfvén speed that is assumed to exist there (due to a significant change in density over a relatively short length scale). Resonances are expected to occur at frequencies of $f = nv_A/2L$, where $n = 1, 2, \ldots$ (e.g., Ionson 1982; Hollweg 1984). The typical length of the loops in which we analyze the wave events is $\sim$400 Mm with Alfvén

---

[10] This wave amplification is also found in measurements of nonthermal line widths below $1.3\,R_\odot$ (e.g., Banerjee et al. 1998; Bemporad & Abbo 2012; Hahn et al. 2012), with the large nonthermal line widths thought to be due to the kink waves (McIntosh & De Pontieu 2012; De Moortel & Pascoe 2012; Pant et al. 2019). The apparent wave damping above $1.3R_\odot$ reported by Bemporad & Abbo (2012) and Hahn et al. (2012) is still somewhat a mystery and could be evidence of non-WKB propagation (Pant & Van Doorsselaere 2020) rather than actual wave dissipation.

[11] This formula has been shown to give a reasonable description of the development of phase mixing length scales in both analytical and numerical treatments of the resonant absorption of kink modes (Pascoe et al. 2013; Soler & Terradas 2015).

speeds of $\sim 500\,\mathrm{km\,s^{-1}}$ (Tiwari et al. 2021). This leads to Alfvén travel times $\tau_A \approx 800\,\mathrm{s}$, whereas the timescale related to the wave damping is $\tau_D \approx 3300\,\mathrm{s}$ (for a wave with period 300 s). Hence, in principle, the waves should be able to traverse the loop twice before any significant damping occurs and set up resonant frequencies at $f = 0.625n$ mHz (a number of which should be observable by CoMP if they were present). In contrast, the decayless kink oscillations found in active-region coronal loops are thought to be the resonant oscillations driven through random footpoint motions (Hindman & Jain 2014; Afanasyev et al. 2020) and shown to be standing modes by Anfinogentov et al. (2013).

There are at least two factors at work that may help explain the lack of observed loop resonances and are likely acting in concert. The first is that there will likely be some turbulent dissipation of the waves (e.g., Matthaeus et al. 1999; Dmitruk et al. 2002; van Ballegooijen et al. 2011; Verdini et al. 2012), given that there exist counterpropagating Alfvénic waves along each of the loops. If we are observing the frequencies/ wavelengths associated with the inertial range, then energy transfer would be self-similar and hence is independent of frequency, i.e., with no impact upon the measurement of frequency-dependent damping. Second, there should be some degree of transmission (or leakage) of the waves in the corona to the chromosphere. In principle, both of these phenomena should not, however, inhibit the development of resonances, but would play a role in limiting the amount of energy that can build up in the coronal volume (Verdini et al. 2012).

As noted, previous work that has discussed the development of resonances in coronal loops generally assumes a steep gradient in the Alfvén speed at the transition region or splits the atmosphere into cavities with jumps in Alfvén speed (e.g., Ionson 1982; Hollweg 1984; Verdini et al. 2012). However, it is not evident that this is the case in the quiescent Sun. The notion of a steep density gradient (and hence Alfvén speed gradient) across the transition region is built upon the premise that the atmosphere is in hydrostatic equilibrium. Recent numerical and observational work suggests this is far from the case. The lower atmosphere is known to be replete with shocks (e.g., Leenaarts et al. 2007, 2012) and spicules (e.g., Pereira et al. 2012), which are continually driving chromospheric material into the corona and potentially removing the steep density gradient (e.g., Martínez-Sykora et al. 2017). The time-averaged profile of the density across the transition region could well be different from the classical hydrostatic case, with tentative evidence for this in coronal holes (Weberg et al. 2020). The nonhydrostatic nature of the lower atmosphere could well lead to significantly less wave reflection and prevent the existence of resonant frequencies in the quiescent corona. In contrast, active regions are known to contain much shorter jets, known as dynamic fibrils (De Pontieu et al. 2007), which would not spread the chromospheric material as thinly and potentially leave the Alfvén speed jump at the transition region intact.

It is clear there are still a number of questions remaining about the structure of the solar atmosphere and its impact on wave propagation. We believe incorporating the dynamic nature of the chromosphere and transition region is an important feature for examining wave propagation and subsequent heating in the quiet Sun.

ORCID iDs

Richard J. Morton https://orcid.org/0000-0001-5678-9002
Ajay K. Tiwari https://orcid.org/0000-0001-6021-8712
Tom Van Doorsselaere https://orcid.org/0000-0001-9628-4113
James A. McLaughlin https://orcid.org/0000-0002-7863-624X

References

Afanasyev, A. N., Van Doorsselaere, T., & Nakariakov, V. M. 2020, A&A, 633, L8
Anfinogentov, S., Nisticò, G., & Nakariakov, V. M. 2013, A&A, 560, A107
Anfinogentov, S. A., Nakariakov, V. M., & Nisticò, G. 2015, A&A, 583, A136
Antolin, P., & Van Doorsselaere, T. 2019, FrP, 7, 85
Antolin, P., Yokoyama, T., & Van Doorsselaere, T. 2014, ApJL, 787, L22
Arregui, I., & Goossens, M. 2019, A&A, 622, A44
Arregui, I., & Ramos, A. A. 2011, ApJ, 740, 44
Aschwanden, M. J., de Pontieu, B., Schrijver, C. J., & Title, A. M. 2002, SoPh, 206, 99
Aschwanden, M. J., Fletcher, L., Schrijver, C. J., & Alexander, D. 1999, ApJ, 520, 880
Aschwanden, M. J., Nightingale, R. W., Andries, J., Goossens, M., & Van Doorsselaere, T. 2003, ApJ, 598, 1375
Aschwanden, M. J., & Peter, H. 2017, ApJ, 840, 4
Banerjee, D., Teriaca, L., Doyle, J. G., & Wilhelm, K. 1998, A&A, 339, 208
Bemporad, A., & Abbo, L. 2012, ApJ, 751, 110
Bradshaw, S. J., & Emslie, A. G. 2020, ApJ, 904, 141
Brooks, D. H., Warren, H. P., Ugarte-Urra, I., & Winebarger, A. R. 2013, ApJL, 772, L19
Buchlin, E., & Velli, M. 2007, ApJ, 662, 701
Cargill, P. J., Bradshaw, S. J., & Klimchuk, J. A. 2012, ApJ, 752, 161
Cranmer, S. R., van Ballegooijen, A. A., & Edgar, R. J. 2007, ApJS, 171, 520
De Moortel, I., & Pascoe, D. J. 2012, ApJ, 746, 31
De Pontieu, B., Hansteen, V. H., Rouppe van der Voort, L., van Noort, M., & Carlsson, M. 2007, ApJ, 655, 624
Dmitruk, P., Matthaeus, W. H., Milano, L. J., et al. 2002, ApJ, 575, 571
Edwin, P. M., & Roberts, B. 1983, SoPh, 88, 179
Goddard, C. R., & Nakariakov, V. M. 2016, A&A, 590, L5
Goddard, C. R., Nisticò, G., Nakariakov, V. M., & Zimovets, I. V. 2016, A&A, 585, A137
Goddard, C. R., Pascoe, D. J., Anfinogentov, S., & Nakariakov, V. M. 2017, A&A, 605, A65
Goossens, M. 2008, in IAU Symp., 247, Waves & Oscillations in the Solar Atmosphere: Heating and Magneto-Seismology, ed. R. Erdélyi & C. A. Mendoza-Briceno (Cambridge: Cambridge Univ. Press), 228

Goossens, M., Andries, J., & Aschwanden, M. J. 2002, A&A, 394, L39
Goossens, M., Andries, J., Soler, R., et al. 2012, ApJ, 753, 111
Goossens, M., Erdélyi, R., & Ruderman, M. S. 2011, SSRv, 158, 289
Goossens, M., Terradas, J., Andries, J., Arregui, I., & Ballester, J. L. 2009, A&A, 503, 213
Hahn, M., Landi, E., & Savin, D. W. 2012, ApJ, 753, 36
Harris, C. R., Millman, K. J., van der Walt, S. J., et al. 2020, Natur, 585, 357
Heyvaerts, J., & Priest, E. R. 1983, A&A, 117, 220
Hillier, A., Van Doorsselaere, T., & Karampelas, K. 2020, ApJL, 897, L13
Hindman, B. W., & Jain, R. 2014, ApJ, 784, 103
Hollweg, J. V. 1984, ApJ, 277, 392
Hood, A. W., Ruderman, M., Pascoe, D. J., et al. 2013, A&A, 551, A39
Hunter, J. D. 2007, CSE, 9, 90
Ionson, J. A. 1978, ApJ, 226, 659
Ionson, J. A. 1982, ApJ, 254, 318
Jafarzadeh, S., Solanki, S. K., Gafeira, R., et al. 2017, ApJS, 229, 9
Jain, R., Maurya, R. A., & Hindman, B. W. 2015, ApJL, 804, L19
Karampelas, K., & Van Doorsselaere, T. 2020, ApJL, 897, L35
Leenaarts, J., Carlsson, M., Hansteen, V., & Rutten, R. J. 2007, A&A, 473, 625
Leenaarts, J., Carlsson, M., & Rouppe van der Voort, L. 2012, ApJ, 749, 136
Lemen, J. R., Title, A. M., Akin, D. J., et al. 2012, SoPh, 275, 17
Magyar, N., & Van Doorsselaere, T. 2016, ApJ, 823, 82
Magyar, N., Van Doorsselaere, T., & Goossens, M. 2017, NatSR, 7, 14820
Magyar, N., Van Doorsselaere, T., & Goossens, M. 2019, ApJ, 882, 50
Mann, I. R., Wright, A. N., & Cally, P. S. 1995, JGR, 100, 19441
Martínez-Sykora, J., De Pontieu, B., Hansteen, V. H., et al. 2017, Sci, 356, 1269
Matthaeus, W. H., Zank, G. P., Oughton, S., Mullan, D. J., & Dmitruk, P. 1999, ApJL, 523, L93
McIntosh, S. W., & De Pontieu, B. 2012, ApJ, 761, 138
McIntosh, S. W., de Pontieu, B., Carlsson, M., et al. 2011, Natur, 475, 477
Montes-Solís, M., & Arregui, I. 2020, A&A, 640, L17
Morton, R. J., Mooroogen, K., & Henriques, V. M. J. 2021, RSPTA, 379, 20200183
Morton, R. J., Tomczyk, S., & Pinto, R. 2015, NatCo, 6, 7813
Morton, R. J., Tomczyk, S., & Pinto, R. F. 2016, ApJ, 828, 89
Morton, R. J., Verth, G., Hillier, A., & Erdélyi, R. 2014, ApJ, 784, 29
Morton, R. J., Verth, G., McLaughlin, J. A., & Erdélyi, R. 2012, ApJ, 744, 5
Morton, R. J., Weberg, M. J., & McLaughlin, J. A. 2019, NatAs, 3, 223
Nakariakov, V. M., & Kolotkov, D. Y. 2020, ARA&A, 58, 441
Nakariakov, V. M., Ofman, L., Deluca, E. E., Roberts, B., & Davila, J. M. 1999, Sci, 285, 862
Nechaeva, A., Zimovets, I. V., Nakariakov, V. M., & Goddard, C. R. 2019, ApJS, 241, 31
Nisticò, G., Nakariakov, V. M., & Verwichte, E. 2013, A&A, 552, A57
Okamoto, T. J., & De Pontieu, B. 2011, ApJL, 736, L24
Pagano, P., & De Moortel, I. 2019, A&A, 623, A37
Pagano, P., & Moortel, I. D. 2017, A&A, 601, A107
Pagano, P., Moortel, I. D., & Morton, R. J. 2020, A&A, 643, A73
Pant, V., Magyar, N., Van Doorsselaere, T., & Morton, R. J. 2019, ApJ, 881, 95
Pant, V., & Van Doorsselaere, T. 2020, ApJ, 899, 1

Pascoe, D. J., Anfinogentov, S. A., Goddard, C. R., & Nakariakov, V. M. 2018, ApJ, 860, 31
Pascoe, D. J., Hood, A. W., de Moortel, I., & Wright, A. N. 2012, A&A, 539, A37
Pascoe, D. J., Hood, A. W., De Moortel, I., & Wright, A. N. 2013, A&A, 551, A40
Pascoe, D. J., Wright, A. N., De Moortel, I., & Hood, A. W. 2015, A&A, 578, A99
Pascoe, D. J., Wright, A. N., & Moortel, I. D. 2010, ApJ, 711, 990
Pedregosa, F., Varoquaux, G., Gramfort, A., et al. 2011, J. Mach. Learn. Res., 12, 2825
Pereira, T. M., De Pontieu, B., & Carlsson, M. 2012, ApJ, 759, 18
Perez, F., & Granger, B. E. 2007, CSE, 9, 21
Pritchett, P. L., & Dawson, J. M. 1978, PhFl, 21, 516
Ramos, A. A., & Arregui, I. 2013, A&A, 554, A7
Ruderman, M. S., & Roberts, B. 2002, ApJ, 577, 475
Shoda, M., Suzuki, T. K., Asgari-Targhi, M., & Yokoyama, T. 2019, ApJL, 880, L2
Shoda, M., Yokoyama, T., & Suzuki, T. K. 2018, ApJ, 853, 190
Soler, R., & Terradas, J. 2015, ApJ, 803, 43
Spruit, H. C. 1982, SoPh, 75, 3
Terradas, J., Andries, J., Goossens, M., et al. 2008, ApJL, 687, L115
Terradas, J., & Arregui, I. 2018, RNAAS, 2, 196
Terradas, J., Goossens, M., & Verth, G. 2010, A&A, 524, A23
Thurgood, J. O., Morton, R. J., & McLaughlin, J. A. 2014, ApJL, 790, L2
Tiwari, A. K., Morton, R. J., & McLaughlin, J. A. 2021, ApJ, 919, 74
Tiwari, A. K., Morton, R. J., Régnier, S., & McLaughlin, J. A. 2019, ApJ, 876, 106
Tomczyk, S., Card, G. L., Darnell, T., et al. 2008, SoPh, 247, 411
Tomczyk, S., & McIntosh, S. W. 2009, ApJ, 697, 1384
Tomczyk, S., McIntosh, S. W., Keil, S. L., et al. 2007, Sci, 317, 1192
van Ballegooijen, A. A., Asgari-Targhi, M., Cranmer, S. R., & DeLuca, E. E. 2011, ApJ, 736, 3
van Ballegooijen, A. A., Asgari-Targhi, M., & Voss, A. 2017, ApJ, 849, 46
Van Doorsselaere, T., Brady, C. S., Verwichte, E., & Nakariakov, V. M. 2008, A&A, 491, L9
Van Doorsselaere, T., Goossens, M., Magyar, N., Ruderman, M. S., & Ismayilli, R. 2021, ApJ, 910, 58
Van Doorsselaere, T., Li, B., Goossens, M., Hnat, B., & Magyar, N. 2020, ApJ, 899, 100
Verdini, A., Grappin, R., & Velli, M. 2012, A&A, 538, A70
Verth, G., Terradas, J., & Goossens, M. 2010, ApJL, 718, L102
Verwichte, E., Nakariakov, V. M., Ofman, L., & Deluca, E. E. 2004, SoPh, 223, 77
Verwichte, E., Van Doorsselaere, T., White, R. S., & Antolin, P. 2013, A&A, 552, A138
Virtanen, P., Gommers, R., Oliphant, T. E., et al. 2020, NatMe, 17, 261
Waskom, M. & the seaborn development team 2020, mwaskom/seaborn, Zendo, doi:10.5281/zenodo.592845
Weberg, M. J., Morton, R. J., & McLaughlin, J. A. 2018, ApJ, 852, 57
Weberg, M. J., Morton, R. J., & McLaughlin, J. A. 2020, ApJ, 894, 79
Williams, T., Walsh, R. W., Winebarger, A. R., et al. 2020, ApJ, 892, 134
Yang, Z., Bethge, C., Tian, H., et al. 2020, Sci, 369, 694